Computational Energy Science

Vol. 2, No. 2, p. 1-17, 2025

Original article

A modified generalized continuous surface tension force model for the *N*-component immiscible and incompressible fluid flows by phase-field method

Sheng Su[1], Junxiang Yang[1]*

[1]*School of Computer Science and Engineering, Faculty of Innovation Engineering, Macau University of Science and Technology, Macao 999078, P. R. China*

Keywords:
N-component fluid flows
surface tension force
phase-field model
spurious velocity

Cited as:
Su, S., Yang, J. A modified generalized continuous surface tension force model for the *N*-component immiscible and incompressible fluid flows by phase-field method. Computational Energy Science, 2025, 2(2): 1-17.
https://doi.org/10.46690/compes.2025.02.01

Abstract:
In this work, we present a novel continuous surface tension force model for the phase-field model for *N*-component immiscible and incompressible fluid flows. The multi-phase Cahn-Hilliard-Navier-Stokes phase-field system is used to describe the evolutions of interfaces, velocities, and pressure. In phase-field model, the concentration of fluid smoothly changes from one fluid to other fluids, this transition region has finite thin thickness across fluid interface. Within the transition region, the surface tension force works. The force magnitude is assumed to be proportional to the interfacial curvature times a smoothed Dirac delta function, the force direction is determined by the unit normal vector to interface. With the fluid concentration (or phase-field function), we derive the associated signed-distance function from the equilibrium interface condition. The curvature is accurately calculated with the signed-distance function instead of the phase-field function. Moreover, the unit normal vector to interface and smoothed Dirac delta function are also calculated based on the signed-distance function. The proposed model is general in the sense that the interactions between arbitrary *N* components can be achieved without specific criterions. Compared with the continuous surface tension model based on phase-field function, the present model can significantly suppress the evolution of spurious velocity as the thickness of diffuse interface becomes sharp. The numerical simulations, such as pressure jump, spurious velocity, liquid lens, rising bubble in a four-component fluid system, and droplet impacting on a thin liquid film, are implemented to validate the capability of the proposed model.

1. Introduction

The multi-component immiscible fluid flows generally includes the complex interactions among different fluid interfaces. In many engineering or scientific fields, the interfacial hydrodynamics of multiple fluids plays an increasingly important role. In boiling water reactor, the vapor/liquid phase change requires the researchers to accurately capture the two-phase interface evolution (Wang et al., 2021; Chen et al., 2024). In the bio-medical engineering, the delivery of liquid drug depends on the researches of single emulsion and double emulsion which are related to topology changes of interfaces (Rosca et al., 2004; Nightingale et al., 2014; Setu et al., 2015; Mu et al., 2023). Moreover, the bubble and droplet behaviours also include complex interfacial dynamics and they are widely investigated in fundamental fluid mechanics, see (Zhu et al., 2022; Zhang et al., 2023; Bi et al., 2024; Wang et al., 2024) for some typical studies.

Unlike the front tracking (Tryggvason et al., 2001), immersed boundary (Li et al., 2013), and immersed interface (Xiao et al., 2021) methods, the conservative level set method and phase-field method are more efficient and practical in multi-phase fluid simulations. The main reasons are: (i) the mass conservation of fluid system is satisfied in the mixed-fluid sense; (ii) the topology changes, such as the coalescence and

Yandy Scientific Press

*Corresponding author.
E-mail address: 2240003913@student.must.edu.mo (S. Su); jxyang@must.edu.mo (J. Yang).

Received April 6, 2025; revised April 21, 2025; accepted June 2, 2025; available online June 7, 2025.

the breakup, can be implicitly captured by solving the governing equations; (iii) the surface tension force on fluid interface is directly added into the momentum equation without explicitly defining the jump condition on interface. It is worth noting that the local fluid mass (i.e., the fluid by thresholding at 0.5 isocontour) may not be conserved for the conservative level-set and phase-field Cahn-Hilliard (CH) models. Moreover, we admit that the surface tension force with a pressure jump formulation (Caltagirone, 2021; Cho and Kang, 2021) can effectively reduce the parasitic currents by orders of magnitude because the surface tension force is automatically discretized in a way consistent with pressure discretization. Although the discretization of continuous surface tension formulation is inconsistent with pressure discretization, its implementation is easier and it has been widely used in numerous fluid simulations. For example, the mostly adopted surface tension force formulation for the conservative level set method is the continuous surface tension force model (Tornberg and Engquist, 2000; Olsson and Kreiss, 2005; Olsson et al., 2007). In this model, the density of surface tension force is proportional to the interfacial curvature times a smoothed Dirac delta function and the force effect is spread into the neighborhood of interface. In recent years, the free energy-based surface tension force models have been developed for the binary and multi-phase conservative level set methods (Yuan et al., 2017; Howard and Tartakovsky, 2021). Based on the continuous surface tension force formulation used in level set method, Kim (2005) proposed a phase-field-based continuous surface tension force model for two-phase incompressible fluid flows. By introducing three fluid concentrations and utilizing the unique decomposition of physical surface tension coefficients, Kim (2007) developed a continuous surface tension force model for ternary phase-field fluid flows.

For two and three-phase fluids, there have been numerous surface tension force models. By introducing an anti-curvature term into the Allen-Cahn type model, Chiu (2019) developed a new conservative phase-field fluid model. In Chiu and Lin's work, the continuous surface tension force model with a Helmholtz smoother was used in simulating raising bubbles and milkcrown problem. To simulate the two-phase flows with unstructured grids, Hwang and Jain (2024) developed a robust phase-field fluid model with continuous surface tension force formulation. To achieve the energy-stable computation, the surface tension force model with a combination of phase-field function and chemical potential gradient was widely adopted. Based on this formulation, Liu et al. (2021) designed an efficient phase-field fluid solver for the two-phase turbulent simulation. Zhao and Han (2021) presented a second-order accurate and unconditionally energy-stable scheme for the Cahn-Hilliard-Navier-Stokes systems. In a recent work, Goulding et al. (2024) proposed a simplified conservative discretization of the Cahn-Hilliard-Navier-Stokes equations and authors addressed various surface tension force formulations in detail for the Cahn-Hilliard-type fluids. Based on a ternary surface tension force formulation, Hong and Zhao (2023) developed an energy-stable time-marching supplementary variable method for three-component Cahn-Hilliard fluids system. Yang et al. (2024) presented a stable and second-order accurate scheme for the L^2 three-phase fluid system by using a generalized time-dependent auxiliary variable approach. However, some models (Zhao and Han, 2021; Hong and Zhao, 2023; Yang et al., 2024) are not trivial to straightforwardly extended into N-component ($N > 3$) fluids. The main reason is the decomposition of physical surface tension coefficient into phase specific surface tension coefficients leads to over-determined problem. Using the physical surface tension coefficients, Dong (2014, 2015) developed N-phase phase-field fluid model from second law of thermodynamics and presented a surface tension force model with the tensor product of the gradients of phase-field functions. This formulation has been used to simulate multi-phase fluid flows in contact with solid wall (Dong, 2017) and with open boundaries (Yang and Dong, 2018). Based on the idea of continuous surface tension force, Kim (2009) originally proposed a generalized surface tension force model for the phase-field fluid flows with arbitrary N components. In Kim's work, an additional regularized Dirac delta function was introduced to spread the force density into the neighborhood of interface. The interfacial curvature was calculated based on the phase-field function of each fluid component. The generalized continuous surface tension force model has been successfully used to simulate various multi-phase fluid flows, see Lee and Kim (2015); Aihara et al. (2023); Xia et al. (2023). The present work focuses on an improved version of Kim's generalized continuous surface force model (Kim, 2009) for N-component phase-field fluid flows.

Based on our experiences for level set method and phase-field method, we observe that the signed-distance function, which is generally used in level set method, performs better in calculate the interfacial curvature. Therefore, a natural approach is to recast the expression of curvature in (Kim, 2009) with signed-distance function. In this work, we first give the expression of signed-distance function with phase-field function and equilibrium interface condition. We accurately calculate the curvature of each fluid interface with the associated signed-distance function. The unit normal vector to interface and gradient of interface are also calculated with signed-distance function. A hybrid smoothed Dirac delta with phase-field function and signed-distance function is used to spread the force density into diffuse interface region. The proposed continuous surface tension force model can be easily derived by modifying some expressions in Kim's model (Kim, 2009). The numerical results will show that the present model leads to more accurate curvature calculation and significantly suppresses the increase of spurious velocity when then diffuse interface becomes sharp. Moreover, the numerical test of a liquid lens will indicate that the present model well simulate the spreading length of a liquid lens, the present values are comparable to the previous values obtained by conservative level set method (Howard and Tartakovsky, 2021). To validate the capability of present model, we will implement the simulations of rising bubble and droplet impacting on a thin liquid film. The proposed model is straightforward and practical in various multi-phase fluid simulation. It is worth noting that any effective numerical algorithm can be used to perform the calculation.

The rest parts of this work are organized as follows.

In Section 2, we first briefly review the phase-field fluid method and Kim's surface tension force model. Then, an improved surface tension force model is introduced. In Section 3, a simple and practical time-marching scheme is described. The numerical experiments are implemented in Section 4 to validate the proposed model. The conclusions are drawn in Section 5.

2. Surface tension force models for phase-field method

In this section, we first briefly review a generalized continuous surface tension force model which was proposed by Kim (2009). Then, we present the motivation and propose an improved form of generalized continuous surface model for the phase-field models for N-component ($N \geq 3$) immiscible and incompressible fluid flows.

2.1 Previous continuous surface tension force model

In the domain Ω, we define a phase-field function $\phi = \phi(\mathbf{x},t)$, where $\mathbf{x}$ and t are spatial and temporal variables. This phase-field function ϕ can be used to represent the fluid concentration. In one fluid component, we set $\phi = 1$. In another fluid, we set $\phi = 0$. Across the interface between two fluids, ϕ smoothly changes from 0 to 1. The fluid interface is represented by the 0.5-level set of ϕ. A schematic illustration is shown in Fig. 1.

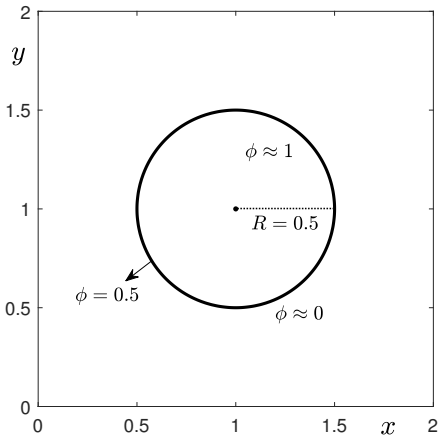

Fig. 1. Schematic illustration of two immiscible fluids with an interface. The concentration of one fluid is represented by ϕ.

For a fluid system consists of arbitrary N components ($N \geq 3$), the concentration of i-th fluid component can be represented by a phase-field function ϕ_i. In the interior and exterior of i-th fluid components, we let $\phi_i = 1$ and 0, respectively. From Kim (2009), the interfacial dynamics of multiple fluids can be described by the following N-component Cahn-Hilliard-Navier-Stokes (CHNS) system:

$$\frac{\partial \phi_i}{\partial t} + \nabla \cdot (\mathbf{u}\phi_i) = \frac{1}{Pe}\Delta \mu_i \tag{1}$$

$$\mu_i = F'(\phi_i) - \varepsilon^2 \Delta \phi_i + \beta(\phi) \tag{2}$$

$$\rho(\phi)\left(\frac{\partial \mathbf{u}}{\partial t} + \mathbf{u}\cdot\nabla\mathbf{u}\right) = -\nabla p + \frac{1}{Re}\nabla\cdot\left[\eta(\phi)(\nabla\mathbf{u} + \nabla\mathbf{u}^T)\right] + \mathrm{SF}(\phi) + \frac{\rho(\phi)}{Fr^2}\mathbf{g} \tag{3}$$

$$\nabla \cdot \mathbf{u} = 0 \tag{4}$$

Here $i = 1, 2, \cdots, N$, μ_i is the chemical potential of i-fluid component, $F(\phi_i) = 0.25\phi_i^2(1-\phi_i)^2$ is a double-well potential which contributes to phase separation, $F'(\phi_i) = dF(\phi_i)/d\phi_i$ is the derivative of $F(\phi_i)$ with respect to ϕ_i. The thickness of diffuse interface across fluid interface is related to a small constant ε. To satisfy the hyperlink condition $\phi_1 + \phi_2 + \cdots + \phi_N = 1$, a particular choice of Lagrange multiplier is $\beta(\phi) = -\frac{1}{N}\sum_{i=1}^{N} F'(\phi_i)$ (Kim, 2009). The velocity of fluid is $\mathbf{u}$. In two-dimensional (2D) or three-dimensional (3D) space, the velocity components are (u,v) or (u,v,w). The fluid pressure is p. The gravitational acceleration is $\mathbf{g}$. Let ρ_i and η_i be the density and viscosity of i-fluid component, the global density and viscosity functions are defined as:

$$\rho(\phi) = \rho_1\phi_1 + \rho_2\phi_2 + \ldots + \rho_{N-1}\phi_{N-1} + \rho_N\phi_N \tag{5}$$

$$\eta(\phi) = \eta_1\phi_1 + \eta_2\phi_2 + \ldots + \eta_{N-1}\phi_{N-1} + \eta_N\phi_N \tag{6}$$

Let L_c, U_c, ρ_c, μ_c, and η_c be the characteristic length, velocity, density, chemical potential, and viscosity, respectively. The dimensionless numbers are Reynolds number $Re = \rho_c U_c L_c/\eta_c$, Peclect number $Pe = U_c L_c/(M\mu_c)$, Froude number $Fr = U_c^2/(gL_c)$. For a fluid system consists of three components, the surface tension coefficient on interface, σ_{ij}, can be decomposed into the phase specific surface tension coefficients σ_1, σ_2, and σ_3 such that:

$$\sigma_{12} = \sigma_1 + \sigma_2,\ \sigma_{13} = \sigma_1 + \sigma_3,\ \sigma_{23} = \sigma_2 + \sigma_3 \tag{7}$$

This decomposition is uniquely defined as $\sigma_1 = (\sigma_{12} + \sigma_{13} - \sigma_{23})/2$, $\sigma_2 = (\sigma_{12} + \sigma_{23} - \sigma_{13})/2$, and $\sigma_3 = (\sigma_{13} + \sigma_{23} - \sigma_{12})/2$. These phase specific surface tension coefficients are used to construct a continuous surface tension force formulation (Kim, 2007). It is worth noting that the values of σ_{12}, σ_{13}, and σ_{23} are not arbitrarily chosen. We need to properly set their values such that $\sigma_1 > 0$, $\sigma_2 > 0$, and $\sigma_3 > 0$. However, for a fluid system which includes more than three components, Kim (2009) pointed out that the unique decomposition did not exist. For example, a four-component fluid system may lead to:

$$\sigma_{12} = \sigma_1 + \sigma_2,\ \sigma_{13} = \sigma_1 + \sigma_3,\ \sigma_{14} = \sigma_1 + \sigma_4 \tag{8}$$

$$\sigma_{23} = \sigma_2 + \sigma_3,\ \sigma_{24} = \sigma_2 + \sigma_4,\ \sigma_{34} = \sigma_3 + \sigma_4 \tag{9}$$

It is obvious that the above mentioned system is over-determined. To overcome this problem, Kim (2009) developed a generalized continuous surface tension force model as:

$$\mathbf{SF}(\phi) = \sum_{i=1}^{N-1}\left(\sum_{j=i+1}^{N}\frac{\sigma_{ij}}{2}\left[\mathbf{sf}(\phi_i) + \mathbf{sf}(\phi_j)\right]\delta(\phi_i,\phi_j)\right) \tag{10}$$

where $\delta(\phi_i,\phi_j) = 5\phi_i\phi_j$ is a function which combines two fluids and

$$\mathbf{sf}(\phi_i) = -\alpha\varepsilon\nabla\cdot\left(\frac{\nabla\phi_i}{|\nabla\phi_i|}\right)|\nabla\phi_i|\nabla\phi_i$$

The dimensionless Weber number can be defined as $We_{ij} = \rho_c L_c U_c^2/\sigma_{ij}$. To match the surface tension of sharp interface model, α should satisfies:

$$\int_{-\infty}^{\infty} \varepsilon\alpha|\phi_x^{\text{eq}}|^2\, dx = 1 \tag{11}$$

where $\phi_x^{\text{eq}} = 0.5(1+\tanh(x/(2\sqrt{2}\varepsilon)))$. Thus, we obtain $\alpha = 6\sqrt{2}$. For more descriptions of this surface tension force model, please refer to Kim (2009). We note that Eq. (11) only holds for a planar interface. Since it is hard for us to determine α from the equilibrium state of a circle or a sphere interface, we only approximately calculate α by referring previous works (Kim, 2005, 2007, 2009).

2.2 An improved continuous surface tension force model

By adding an anti-curvature term into the Allen-Cahn (AC) model, Chiu and Lin (2011) developed a conservative phase-field model for the incompressible two-phase fluid simulation. In their work, the curvature was computed using a phase-field function, i.e.,

$$\text{Curvature} = \nabla\cdot\left(\frac{\nabla\phi}{|\nabla\phi|}\right) \tag{12}$$

where ϕ changes from 0 to 1 in different fluids. Note this curvature calculation was also used in Kim (2005) for a continuous surface tension force model for a phase-field model. Recently, Jain (2022) observed that if the unit normal vector to interface was calculated with a signed-distance function instead of a phase-field function, the resulting model not only captured the interface well but also reduced the spurious velocity around a stationary droplet. Mathematically, we have:

$$\mathbf{n}_\Gamma = \frac{\nabla\phi}{|\nabla\phi|} = \frac{\nabla\psi}{|\nabla\psi|} \tag{13}$$

where $\mathbf{n}_\Gamma$ is the unit normal vector to the fluid interface and ψ is a signed-distance function. For an equilibrium interface of phase-field equation, we have $|\nabla\phi| = \phi(1-\phi)/(\sqrt{2}\varepsilon)$ (Li et al., 2016). Let s be a coordinate along fluid interface normal, the following equality is obtained as $\phi\to 0$ and $s\to-\infty$:

$$\frac{d\phi}{ds} = \frac{\phi(1-\phi)}{\sqrt{2}\varepsilon} \tag{14}$$

Let ψ be a signed-distance function from fluid interface, such that $\psi(\phi) = s(\phi) - s(\phi=0.5)$. Then, we can recast Eq. (14) to be:

$$\frac{d\phi}{d\psi} = \frac{\phi(1-\phi)}{\sqrt{2}\varepsilon} \tag{15}$$

At $\psi = 0$, we have $\phi = 0.5$. Integrating Eq. (14), we derive:

$$\phi = \frac{e^{(\psi/\varepsilon)}}{1+e^{(\psi/\varepsilon)}} \tag{16}$$

Thus, the signed-distance function ψ can be calculated from:

$$\psi = \sqrt{2}\varepsilon\ln\left(\frac{\phi}{1-\phi}\right) \approx \sqrt{2}\varepsilon\ln\left(\frac{\phi+\chi}{1-\phi+\chi}\right) \tag{17}$$

Here, we set χ = 1e-10. In the proposed method, we need to reinitialize ψ from the above equation in each time level. Since the update ψ is explicit, this step will not leads to obvious CPU time costs. When the phase-field is close to zero, we introduce a small χ to avoid the singularity. We note that an arbitrarily small constant within the limits of machine error can be used as the value of χ, the numerical simulations in Section 4 will indicate that the proposed formulation can work well. In Fig. 2, we plot the one dimensional profiles of phase-field function ϕ and the signed-distance function ψ.

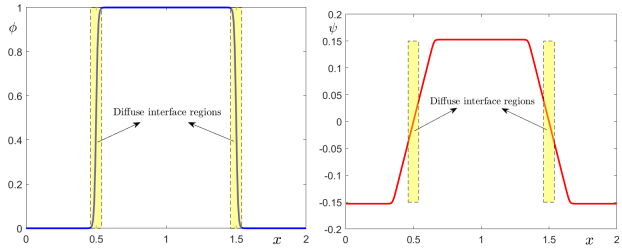

Fig. 2. Schematic illustrations of the one dimensional profiles of phase-field function ϕ (Left) and the signed-distance function ψ (Right).

In present work, we calculate the curvature with signed-distance function, i.e.,

$$\text{Curvature} = \nabla\cdot\left(\frac{\nabla\psi}{|\nabla\psi|}\right) \tag{18}$$

To show the merit of this approach, we consider a stationary droplet with radius R = 0.5 in domain $\Omega = (0,2)\times(0,2)$ (see Fig. 1). Theoretically, the mean curvature of a circular droplet should be $1/R$ = 2. We implement the numerical computations of curvature using Eqs. (12) and (18). The fine enough mesh size 1024×1024 is used. Fig. 3 shows the numerical curvatures. The maximum magnitudes of curvature computed with Eqs. (12) and (18) are 2.2921 and 2.0281, respectively. We observe that Eq. (18) is indeed more accurate than Eq. (12). Therefore, we will use Eq. (18) and $\nabla\psi$ to calculate the curvature and gradient on fluid interface.

For a multi-component fluid system, the curvature of i-th fluid interface can be expressed as:

$$\text{Curvature}_i = \nabla\cdot\left(\frac{\nabla\psi_i}{|\nabla\psi_i|}\right), \quad i = 1,2,...,N \tag{19}$$

where ψ_i represents the signed-distance function calculated by i-fluid component. Using $\nabla\psi_i$ and $|\nabla\psi_i|$ to replace $\nabla\phi_i$ and $|\nabla\phi_i|$, we present the following new continuous surface tension model:

$$\mathbf{SF}(\phi,\psi) = \sum_{i=1}^{N-1}\left(\sum_{j=i+1}^{N}\frac{\xi\sigma_{ij}}{2}\left[\mathbf{sf}(\psi_i)+\mathbf{sf}(\psi_j)\right]\delta(\phi_i,\phi_j)\right) \tag{20}$$

where

$$\mathbf{sf}(\psi_i) = -\alpha\varepsilon\nabla\cdot\left(\frac{\nabla\psi_i}{|\nabla\psi_i|}\right)|\nabla\psi_i|\nabla\psi_i$$

Here, $\alpha = 6\sqrt{2}$, ξ is a scaling parameter to meet the pressure jump in specific cases. Similar with the description in Kim (2009), the term $5\alpha\varepsilon\phi_i\phi_j|\nabla\psi_i|^2$ works as a smoothed

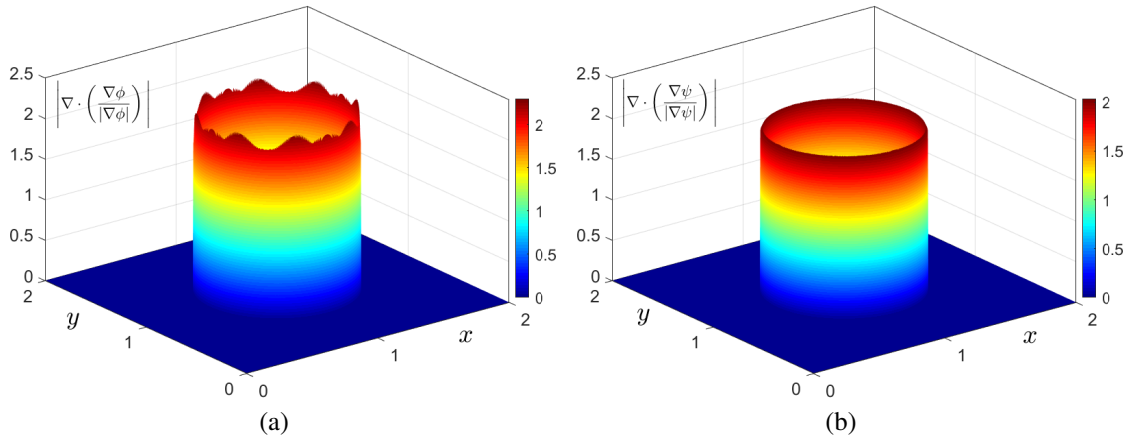

Fig. 3. Schematic illustrations of curvatures computed with (a) Eq. (12) and (b) Eq. (18).

Dirac delta function. In Fig. 4, we present a one dimensional schematic illustration, where $\phi = 0.5(1+\tanh(x/(2\sqrt{2}\varepsilon)))$ with $\varepsilon = 0.1$ is plotted with dashed line. For this binary system, the smoothed Dirac delta function $5\alpha\varepsilon\phi(1-\phi)|\nabla\psi|^2$ is plotted with solid line. In Section 4, several numerical experiments will be implemented to verify the advantages of present model (i.e., Eq. (20)) in suppressing spurious velocity, especially when the diffuse interface becomes sharp.

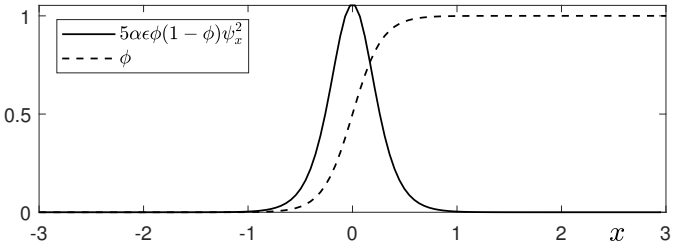

Fig. 4. Schematic illustration of one dimensional profiles of ϕ and $5\alpha\varepsilon\phi(1-\phi)|\nabla\psi|^2$.

3. Numerical solution algorithm

Since the present work only aims to present a new continuous surface tension force model for a N-component fluid system, we do not pay more attentions to design high-performance (i.e., strongly stable, high-order accurate, structure-preserving) numerical methods. A simplest and practical numerical solver is used to calculate the CHNS system. For the incompressible NS equation, a first-order time-accurate projection method is used. For the N-component CH equations, we adopt a first-order time-accurate linear implicit-explicit scheme with stabilization. The finite difference method (FDM) is used to implement spatial discretization. For the Laplacian term, the second-order central difference scheme is used. For the advection terms in the NS equations and CH equations, we discretize them with second-order ENO scheme (Kim, 2005) and central difference scheme. Please refer to Kim (2012); Zhu et al. (2020) for more details of the spatial schemes based on FDM. Let $(\cdot)^n$ be an approximation of $(\cdot)$ at $t = n\Delta t$, where $\Delta t = T/N_t$ is the uniform time step, T is the total computational time, N is the number of time iteration. We present a time-marching semi-discrete scheme as follows:

$$\frac{\mathbf{u}^*-\mathbf{u}^n}{\Delta t}+\mathbf{u}^n\cdot\nabla\mathbf{u}^n=\frac{1}{\rho(\phi^n)}\left(\frac{1}{Re}\nabla\cdot\left[\eta(\phi^n)(\nabla\mathbf{u}+\nabla\mathbf{u}^T)^n\right]+\mathrm{SF}(\phi^n)\right)+\frac{1}{Fr^2}\mathbf{g} \tag{21}$$

$$\frac{\mathbf{u}^{n+1}-\mathbf{u}^*}{\Delta t}=-\frac{1}{\rho(\phi^n)}\nabla p^{n+1} \tag{22}$$

$$\nabla\cdot\mathbf{u}^{n+1}=0 \tag{23}$$

$$\frac{\phi_i^{n+1}-\phi_i^n}{\Delta t}+\nabla\cdot(\mathbf{u}^n\phi_i^n)=\frac{1}{Pe}\Delta\mu_i^{n+1} \tag{24}$$

$$\mu_i^{n+1}=F'(\phi_i^n)-\varepsilon^2\Delta\phi_i^{n+1}+\beta(\phi^n)+\lambda(\phi_i^{n+1}-\phi_i^n) \tag{25}$$

$$\phi_N^{n+1}=1-\sum_i^{N-1}\phi_i^{n+1} \tag{26}$$

Here $i = 1,2,\cdots,N-1$, $\mathbf{u}^*$ is an intermediate velocity which does not satisfy the divergence-free condition. The last term in Eq. (25) is introduced to improve the stability, $\lambda > 0$ is a stabilization parameter. In each time iteration, we explicitly update $\mathbf{u}^*$ from Eq. (21). To update the pressure, we take the divergence operation to Eq. (22) and obtain:

$$\nabla\cdot\left(\frac{1}{\rho(\phi^n)}\nabla p^{n+1}\right)=\frac{1}{\Delta t}\nabla\cdot\mathbf{u}^* \tag{27}$$

where the divergence-free condition in Eq. (23) is used. The pressure is updated by iteratively solving the above Poisson equation with variable coefficients. The new velocity can be explicitly calculated from Eq. (22). By iteratively solving the coupled Eqs. (24) and (25), we update ϕ_i^{n+1} for $i = 1,2,\cdots,N-1$. Using the hyperlink condition, i.e., $\sum_{i=1}^N \phi_i^{n+1} = 1$, the phase-field function of N-th component is directly updated from Eq. (26). In present work, all iteration computations are achieved by using the linear multigrid algorithm with Gauss-Seidel-type relaxation (Trottenberg et al., 1998).

Remarks. In this work, the main scientific contribution is a new surface tension force model. For the purpose of convenience, the simplest fluid equations with variable density ratio is adopted and the temporally first-order accurate explicit scheme is used to update the intermediate velocity. In our

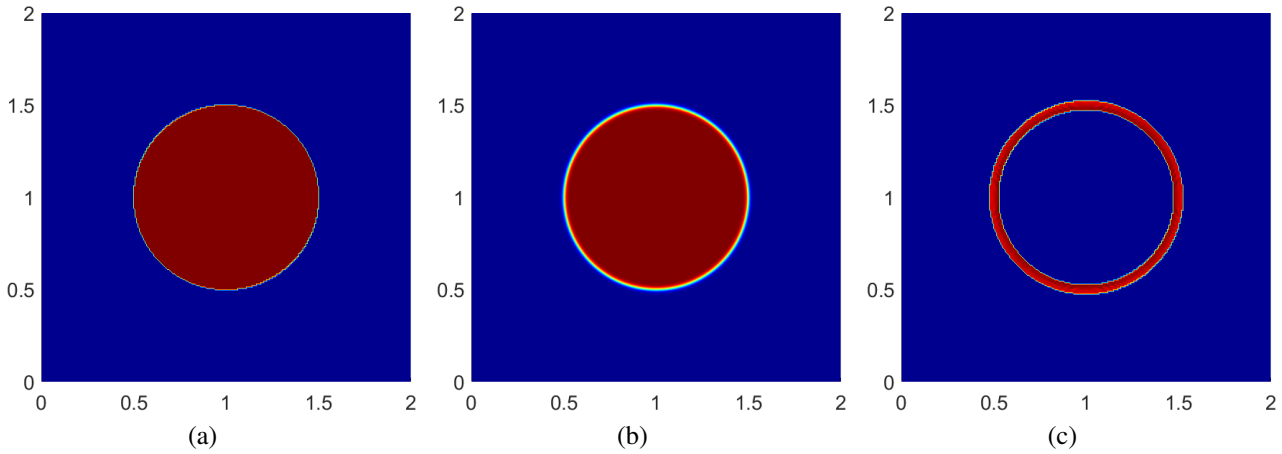

Fig. 5. Initial state of ϕ_1, steady state of ϕ_1, and the curvature at steady state are shown in (a), (b), and (c), respectively.

future works, more precise fluid model with variable densities (Goulding et al., 2024) will be considered. To improve the accuracy and stability, the temporally second-order accurate semi-implicit schemes will be developed.

4. Numerical experiments

In this section, we validate the merit of present model in suppressing spurious velocity as the decrease of thickness of diffuse interface. Moreover, the capabilities are investigated via the simulations of liquid lens, raising bubble, and droplet impacting on thin liquid film. Unless otherwise specified, the periodic boundary condition is used for all variables along x-direction. On the top and bottom boundaries, the velocities are zero, the homogeneous-Neumann boundary condition is used for pressure and phase-field functions. Based on Choi et al. (2009), we define:

$$\varepsilon_m = \frac{mh}{4\sqrt{2}\tanh^{-1}(0.9)} \tag{28}$$

Which indicates that the diffuse interface approximately occupies m grids. The stabilization parameter is $\lambda = 2$.

4.1 Mean curvature of equilibrium profile

To accurately measure the mean curvature of a 2D equilibrium interface profile, we run the simulation with a sharp initial condition into its steady state. The domain is $\Omega = (0,2)\times(0,2)$. Inside a circle region with radius 0.5, we set $\phi_1(x,y,0) = 1$. In the rest region, we set $\phi_1(x,y,0) = 0$. The initial velocity components are set to be zero. In this simulation, we only update ϕ_1 and set $\phi_2(x,y,t) = \phi_3(x,y,t) = 0$. The parameters are h = 1/128, ε_5, $\Delta t = 0.1h$, Re = 100, Pe = 2. The density- and viscosity-matched conditions are used. Fig. 5 displays the initial state of ϕ_1, steady state of ϕ_1, and curvature at steady state. For a circle interface, its exact mean curvature should be 2. The present numerical result of mean curvature is 2.0051. The numerical result and exact result are in good agreement.

4.2 Single stationary droplet

In this example, we simulate a single stationary droplet and plot the L^2 norm and L^∞ norm of spurious current with respect to different mesh sizes. Here, we only calculate ϕ_1 and set ϕ_2 and ϕ_3 be zero all along. Inside the droplet, we let its density and viscosity be ρ_1 and η_1. In the ambient fluid, the density and viscosity are ρ_0 and η_0. The stationary circle droplet with radius 0.2 is placed into the computational domain $\Omega = (0,2)\times(0,2)$. The initial velocity components are zero. We set Re = 100, Δt = 0.001, ε_4, and Pe = 2. Different mesh sizes: 16×16 (h = 1/8), 32×32 (h = 1/16), 64×64 (h = 1/32), 128×128 (h = 1/64), and 256×256 (h = 1/128) are used. The density is set to be 1,000. In case 1, we consider $\eta_1 = \eta_0$ =0 and σ = 1. In case 2, we consider $\eta_1 = \eta_0$ =0.1 and σ = 1. In case 3, we use η_1 = 0.1, η_0 = 0.0001, and σ = 1. In case 4, we use $\eta_1 = \eta_0$ = 0.1 and σ = 10. The simulations stop at t = 1. In Fig. 6, we plot the semi-log views of L^2 norm and L^∞ norm of velocity, respectively. When mesh sizes are not enough, we observe that the L^2 norm and the L^∞ norm of spurious velocity with h = 1/32 are larger than those with h = 1/16. With the refinement of mesh size, it can be observed that the L^2 norm and the L^∞ norm of spurious velocity gradually decrease.

4.3 Three stationary droplets

In this subsection, we investigate the capability of the proposed surface tension force model in suppressing the spurious velocity as the decrease of thickness of diffuse interface. We consider the equilibrium of three droplets places within ambient fluid. In the absence of gravity and other external forces, a stationary droplet should becomes a circle (in 2D space) or a sphere (in 3D space) under the effect of surface tension force. The Laplace formula (Landau and Lifshitz, 1987; Brackbill et al., 1992) gives the relationship between pressure jump and surface tension coefficient of a 2D circular droplet, i.e.,

$$\delta p = \sigma_{ij}\kappa = \frac{\sigma_{ij}}{R} \tag{29}$$

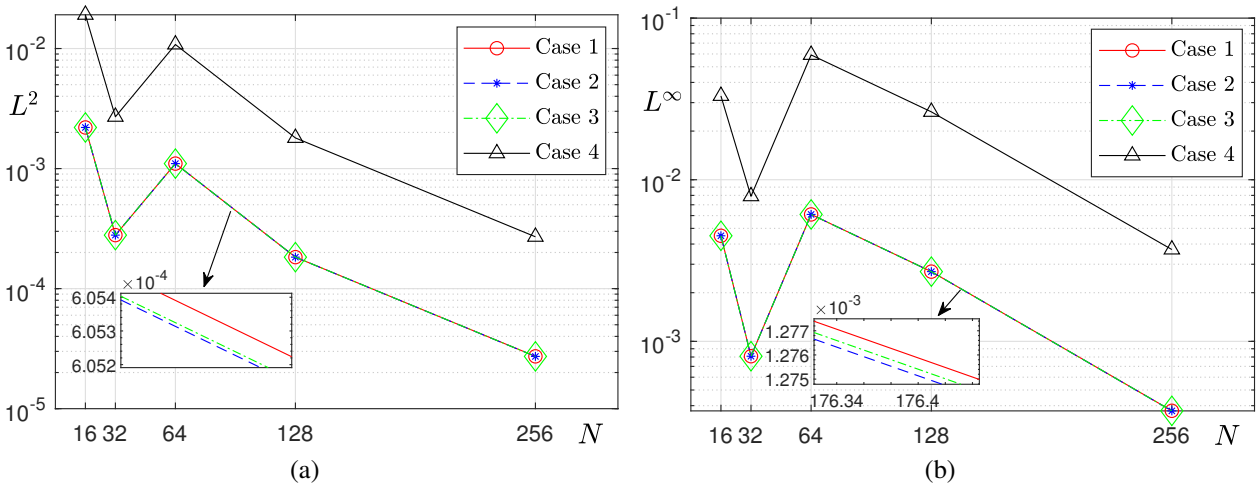

Fig. 6. Semi-log views of (a) L^2 norm and (b) L^∞ norm of spurious velocity. In each figure, the x-axis represents the mesh size, the y-axis represents the norm of spurious velocity.

Here, δp is the pressure jump across the droplet interface, σ_{ij} is the surface tension coefficient on the interface between fluid i and fluid j, κ is the mean curvature, and R is the radius of a circular droplet. The computational domain is set to be $\Omega = (0,8)\times(0,8)$. We uniformly partition the computational domain and set 512 grids in each direction. Thus, h = 1/64. The initial velocities are zero and the initial conditions of three droplets are defined as:

$$\phi_1(x,y,0) = \frac{1}{2}\left[1+\tanh\left(\frac{R-\sqrt{(x-1.6)^2+(y-1.6)^2}}{2\sqrt{2}\varepsilon}\right)\right] \tag{30}$$

$$\phi_2(x,y,0) = \frac{1}{2}\left[1+\tanh\left(\frac{R-\sqrt{(x-4)^2+(y-4)^2}}{2\sqrt{2}\varepsilon}\right)\right] \tag{31}$$

$$\phi_3(x,y,0) = \frac{1}{2}\left[1+\tanh\left(\frac{R-\sqrt{(x-6.4)^2+(y-6.4)^2}}{2\sqrt{2}\varepsilon}\right)\right] \tag{32}$$

The initial condition of ambient liquid can be defined as $\phi_4(x,y,0) = 1-\phi_1(x,y,0)-\phi_2(x,y,0)-\phi_3(x,y,0)$. The radii of three droplets are same and we let R = 0.5. The surface tension coefficients are σ_{14} = 1, σ_{24} = 4, σ_{34} = 2, and σ_{12} = σ_{13} = σ_{23} = 1. The Reynolds number is Re = 1, the Peclect number is Pe = $1/\varepsilon$, and ε = ε_4. The densities and viscosities are matched, the gravity is absent. In the proposed model 20, there is an unknown constant ξ, we first need to determine an appropriate value of ξ. To do this, we compare the pressure jumps computed by present model and Kim's model (Kim, 2009), we adjust ξ until the present pressure jump is similar with Kim's result and exact value. After an empirical value of ξ is determined, the proposed surface tension force model is completed. Fig. 7 shows the equilibrium states of three droplets and the pressure field subtracting its minimum value. In Fig. 8, we display the pressure jumps calculated by present model and Kim's model with respect to different time steps: $\Delta t = 10h^2$, $0.1h^2$, and $0.001h^2$ after once time iteration. The results indicate that the numerical pressure jump and theoretical value are in good agreement even if a larger time step is used.

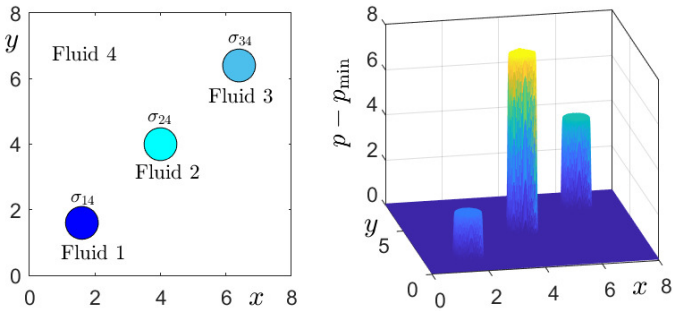

Fig. 7. Equilibrium states of three droplets and the pressure field subtracting its minimum value.

If the droplets are in quiescent conditions, then there are no velocities around the droplets. However, many previous works (Wagner, 2003; Ganesan et al., 2007; Connington and Lee, 2012; Oshima and Tabe, 2015) have showed that the spurious velocity evolved around the equilibrium fluid interfaces. The main reason of spurious velocity is the imbalance between surface tension force and pressure gradient after discretization. In the continuous surface tension model, the surface tension force on fluid interface is converted into a smoothly varying body force that is localized in the neighborhood of interface. Therefore, inaccurate calculations of curvature and gradient may lead to more obvious spurious velocity. To show the merit of present model than Kim's model (Kim, 2009), we gradually let the diffuse interface be sharp and calculate the maximum value of spurious velocity, i.e., $|\mathbf{u}|_{\max}$. Here, ε = ε_4, ε_3, ε_2, and ε_1 are considered. Table 1-3 list the values of $|\mathbf{u}|_{\max}$ calculated by present model and Kim's model (Kim, 2009) with respect to different values of ε and time steps. In Table 1-3, we set Δt = $10h^2$, $0.1h^2$, and $0.001h^2$, respectively. To more intuitively show the results, we plot the values of $|\mathbf{u}|_{\max}$ versus different values of ε in Fig. 9. For ε = ε_4, the proposed model leads to approximately half spurious velocity than that calculated with

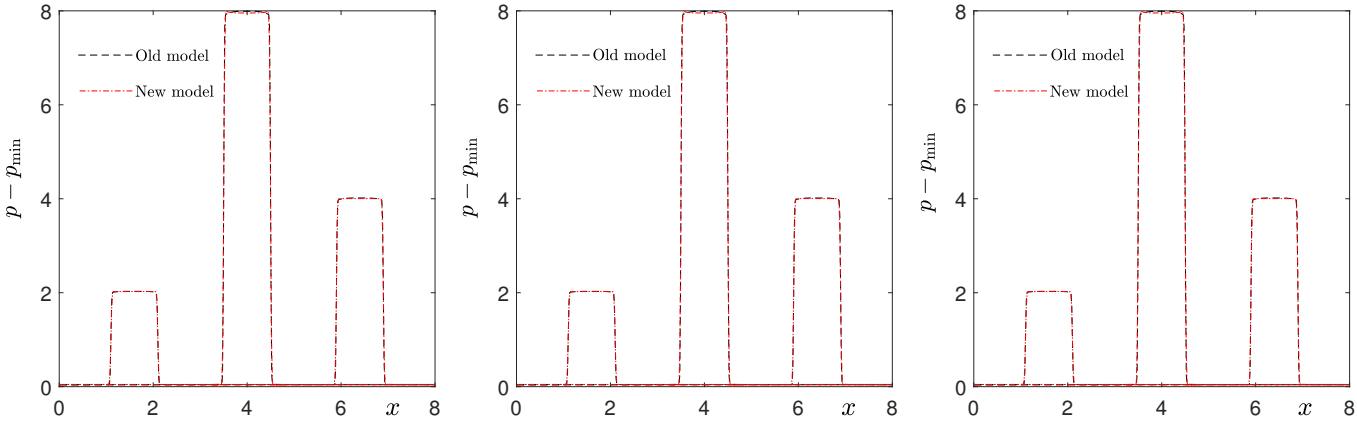

(a) $\Delta t = 10h^2$ (b) $\Delta t = 0.1h^2$ (c) $\Delta t = 0.001h^2$

Fig. 8. Pressure jumps with respect to different time steps. The slice plots of the pressure field are along y = 1.6, y = 4, and y = 6.4. The red dot-and-dash line shows the result calculated by present model. The black dashed line shows the result calculated by Kim's model (Kim, 2009).

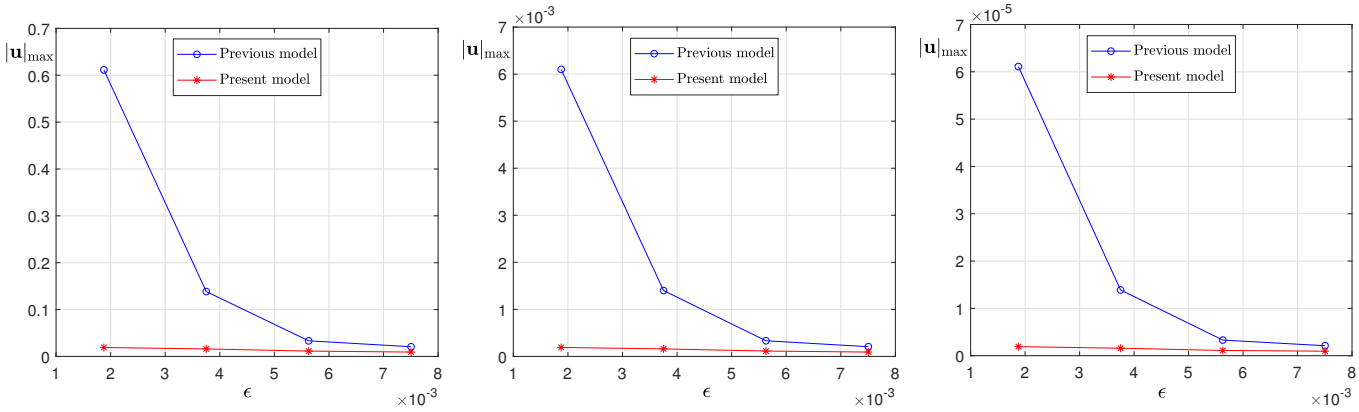

(a) $\Delta t = 10h^2$ (b) $\Delta t = 0.1h^2$ (c) $\Delta t = 0.001h^2$

Fig. 9. Maximum values of spurious velocity with respect to different values of ε.

Kim's model (Kim, 2009). As the diffuse interface becomes sharp, the previous model significantly amplifies the spurious velocity, while the present model obviously delays the increase of spurious velocity.

Table 1. Maximum values of spurious velocity with respect to different values of ε.

	ε_4	ε_3	ε_2	ε_1
Previous model	0.0207	0.0333	0.1384	0.6114
Ratio	2.2258	2.9211	8.6500	32.0105
Present model	0.0093	0.0114	0.0160	0.0191

Next, we implement the simulation of three separated sharp droplets and run the computation into the steady state of phase-field functions. In this test, we set a large Reynolds number Re = 10,000. The initial velocity components are zero. The top row of Fig. 10 shows the initial state and steady state, respectively. In the bottom row of Fig. 10, we plot the curves of L^∞ norm and L^2 norm of velocity. As we can observe, the spurious velocity appears and increases from zero at early stage. With time evolution, both L^∞ norm and L^2 norm of velocity gradually dissipate.

4.4 Convergence test

In this subsection, we perform the convergence test by changing time step and mesh size. The computational domain is $\Omega = (0,1) \times (0,1)$. The initial conditions are set to be:

$$\phi_1(x,y,0) = \frac{1}{2}\left[1 + \tanh\left(\frac{0.1 - \sqrt{(x-0.6)^2 + (y-0.5)^2}}{2\sqrt{2}\varepsilon}\right)\right] \tag{33}$$

$$\phi_3(x,y,0) = \frac{1}{2}\left[1 + \tanh\left(\frac{0.1 - \sqrt{(x-0.4)^2 + (y-0.5)^2}}{2\sqrt{2}\varepsilon}\right)\right] \tag{34}$$

$$\phi_2(x,y,0) = 1 - \phi_1(x,y,0) - \phi_3(x,y,0), u(x,y,0) = v(x,y,0) = 0 \tag{35}$$

Table 2. Maximum values of spurious velocity with respect to different values of ε.

	ε_4	ε_3	ε_2	ε_1
Previous model	2.0702e-4	3.3291e-4	0.0014	0.0061
Ratio	2.2309	2.9113	8.7489	31.9121
Present model	9.2797e-5	1.1435e-4	1.6002e-4	1.9115e-4

Table 3. Maximum values of spurious velocity with respect to different values of ε.

	ε_4	ε_3	ε_2	ε_1
Previous model	2.1095e-6	3.2985e-6	1.3892e-5	6.1105e-5
Ratio	2.2236	2.9864	8.7863	31.9838
Present model	9.4868e-7	1.1045e-6	1.5811e-6	1.9105e-6

The parameters are Re = 100, $\sigma_{12} : \sigma_{13} : \sigma_{23}$ = 1 : 1 : 1, Pe = 2, $\rho_1 = \rho_2 = \rho_3$ = 10, $\eta_1 = \eta_2 = \eta_3$ = 0.1, and ε_4. Three different mesh sizes, i.e., h = 1/64, 1/128, 1/256 are used. The time step is defined as $\Delta t = 0.1h$. All computations stop at t = 1.17. In Fig. 11, the interface profiles of three fluids at t = 1.17 are displayed. When the mesh size is not enough, obvious local mass loss can be observed. We can see that the results converge with the refinement of mesh size and time step.

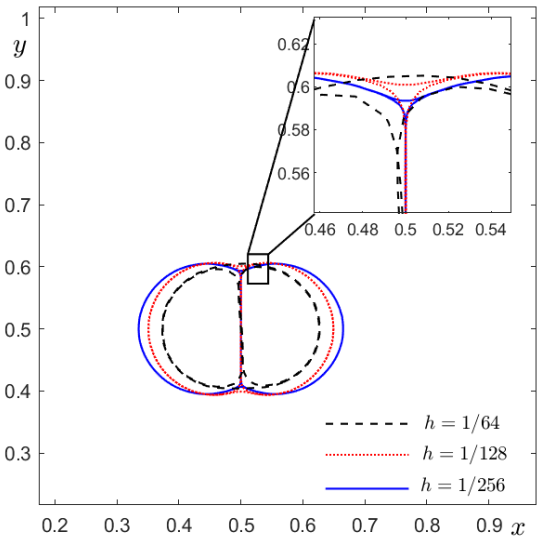

Fig. 11. Interface profiles of three fluids with respect to different mesh sizes and time steps.

4.5 Comparison with different surface tension force models

In this subsection, we compare different surface tension force models by calculating the pressure jump. A stationary circle droplet with radius 0.2 is placed into the domain $\Omega = (0,2)\times(0,2)$. We use the phase-field function ϕ_1 to represent the droplet and set $\phi_2 = \phi_3 = 0$ all along. The initial velocity components are zero. The parameters are defined as h = 1/128, Δt = 0.001, Re = 100, the density ratio and viscosity ratio are 1. In case 1, the present surface tension force model is used. In cases 2-6, the surface tension force models are $\gamma\nabla\cdot(\nabla\phi\otimes\nabla\phi)$ (Di et al., 2008), $\chi\mu\nabla\phi$ (Shen and Yang, 2010), $\sigma\kappa\nabla(g(\phi))$ (Goulding et al., 2024), $\sigma\kappa\nabla\left(\frac{1}{2}(1+\tanh(4\phi-2))\right)$ (Goulding et al., 2024), and $\sigma\kappa\nabla\phi$ (Goulding et al., 2024), respectively. Here, κ is the curvature. Please refer to Goulding et al. (2024) for detailed descriptions of formulations and some parameters. Fig. 12 shows the cross sections of pressure jump after 100 times computations. The exact pressure jump should be 5. The pressure jump computed by the surface tension force model in case 2 deviates far from the exact value. The pressure jumps computed by the present surface tension force model and the other models in cases 3-6 are in good agrement with the exact value.

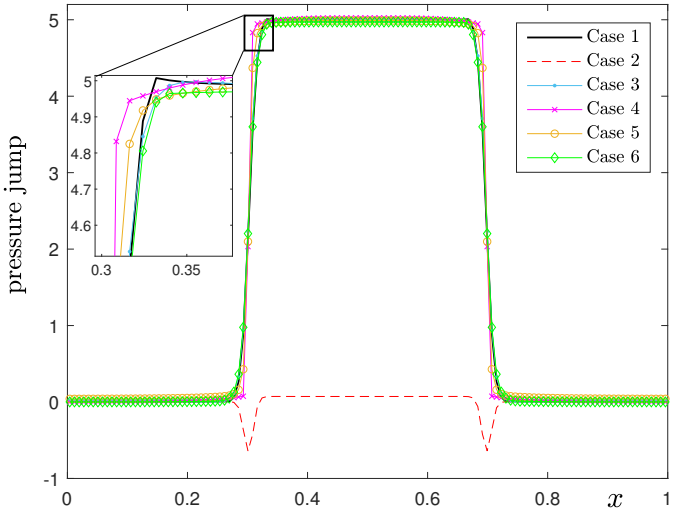

Fig. 12. Pressure jumps computed by the present surface tension force model and previous models.

4.6 Liquid lens in a ternary system

In this subsection, we study the dynamic behaviour of a liquid lens lying on the interface between two immiscible fluids, which is a classic benchmark problem to test the surface tension forces in a ternary fluid system. The simulations are implemented in the computational domain $\Omega = (0,1)\times(0,1)$

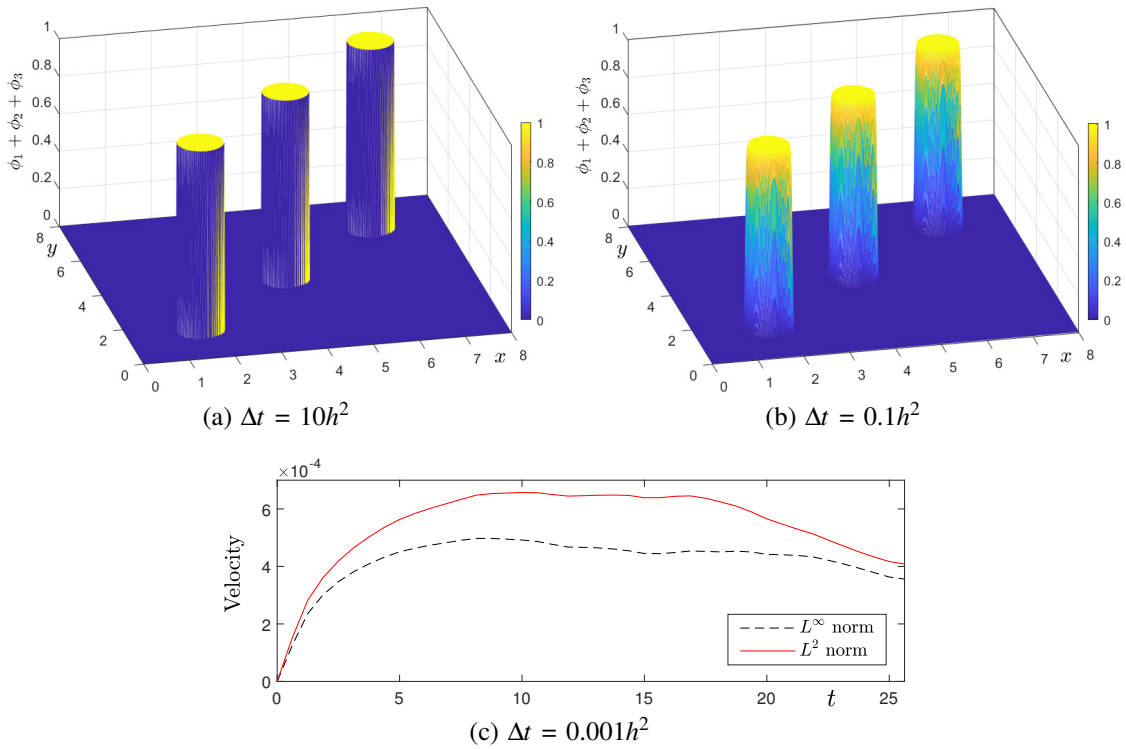

(a) $\Delta t = 10h^2$ (b) $\Delta t = 0.1h^2$

(c) $\Delta t = 0.001h^2$

Fig. 10. The top row shows the initial state and steady state of three separated droplets. The bottom row plots the time evolutions of L^∞ norm and L^2 norm of velocity.

with 128×128 grids. The initial velocities are zero and the initial states of three fluid concentrations are defined as:

$$\phi_1(x,y,0) = \frac{1}{2}\times \left[1+\tanh\left(\frac{\min\left(\sqrt{(x-0.5)^2+(y-0.5)^2}-0.2, y-0.5\right)}{2\sqrt{2}\varepsilon}\right)\right] \tag{36}$$

$$\phi_3(x,y,0) = \frac{1}{2}+ \frac{1}{2}\tanh\left(\frac{-\max\left(-\sqrt{(x-0.5)^2+(y-0.5)^2}+0.2, y-0.5\right)}{2\sqrt{2}\varepsilon}\right) \tag{37}$$

$$\phi_2(x,y,0) = 1-\phi_1(x,y,0)-\phi_3(x,y,0) \tag{38}$$

Fig. 13 shows the initial state. The gravity is absent. We take $\rho_1 = \rho_2 = \rho_3 = 10$ and $\eta_1 = \eta_2 = \eta_3 = 0.1$ which were adopted in Howard and Tartakovsky (2021). The Reynolds number is $Re = 1$, the Peclect number is $Pe = 2$, $\varepsilon = \varepsilon_4$. The time step $\Delta t = 0.1h$ is used. Different surface tension ratios: $\sigma_{12} : \sigma_{13} : \sigma_{23} = 1.4 : 1 : 1.4$, $1.2 : 1 : 1.2$, and $1 : 1 : 1$ are investigated. From Smith et al. (2002), the equilibrium contact angles on triple junctions between three fluid interfaces, denoted by θ_i ($i = 1, 2, 3$), and surface tension coefficients satisfy the following equality:

$$\frac{\sin\theta_1}{\sigma_{23}} = \frac{\sin\theta_2}{\sigma_{13}} = \frac{\sin\theta_3}{\sigma_{12}} \tag{39}$$

The equilibrium length of liquid lens, d, is defined as:

$$\frac{1}{d^2} = \frac{1}{8A}\times \left[\frac{2(\pi-\theta_1)-\sin(2(\pi-\theta_1))}{\sin^2(\pi-\theta_1)}\ \frac{2(\pi-\theta_3)-\sin(2(\pi-\theta_3))}{\sin^2(\pi-\theta_3)}\right] \tag{40}$$

where $A = \pi R^2$ is the initial area of liquid lens, $R = 0.2$ is the initial radius of fluid 2. Fig. 14 shows the equilibrium states of liquid lens with respect to different surface tension coefficients. With the increase of σ_{12} and σ_{23}, we observe that the spreading tendency of liquid lens is suppressed. In Table 4, we list the exact values and numerical values of d with respect to different σ_{12} (or σ_{23}). The N-phase conservative level set method with free energy-based surface tension model (NCLS-FEST) and continuous surface tension model (NCLS-CSF) (Howard and Tartakovsky, 2021) are used to provide numerical contrasts. From the results listed in Table 1, we observe that the numerical values calculated by present surface tension model are in good agreement with exact values NCLS-FEST. The present surface tension model works better in predict the equilibrium length of a liquid lens.

In Fig. 15, we plot the cross sections of equilibrium phase-field functions along $x = 0.5$. Here, 15(a), 15(b), and 15(c) correspond to $\sigma_{12} : \sigma_{13} : \sigma_{23} = 1.4 : 1 : 1.4$, $1.2 : 1 : 1.2$, and $1 : 1 : 1$, respectively. For different surface tension coefficients, we can observe that the numerical results are approximately bounded by 0 and 1.

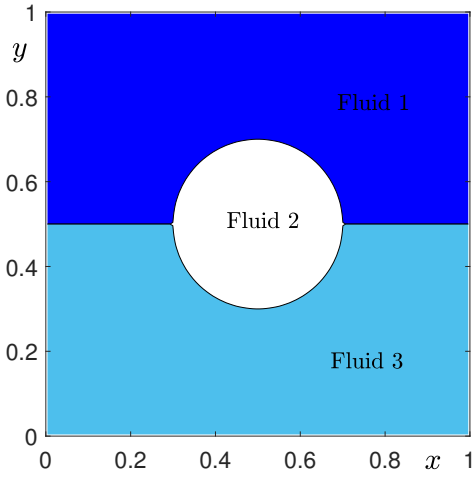

Fig. 13. Initial conditions of liquid lens (fluid 2) lying on the interface between fluid 1 and 3.

4.7 Rising bubble in a four-component system

In this subsection, we investigate the buoyancy-driven rising bubble in a four-component fluid system. By adjusting the surface tension force, we aim to simulate the bubble penetrates the fluid-fluid interface, or remains captured between two fluid layers. The computational domain is set to be $\Omega = (0,1) \times (0,4)$. Along x-direction and y-direction, we set 64 grids and 256 grids, respectively. The initial velocities are zero. The initial conditions of bubble (fluid 1) and rest fluids are defined as:

$$\phi_1(x,y,0) = \frac{1}{2}\left[1+\tanh\left(\frac{0.25-\sqrt{(x-0.5)^2+(y-0.4)^2}}{2\sqrt{2}\varepsilon}\right)\right] \tag{41}$$

$$\phi_2(x,y,0) = \frac{1}{2}\left[1-\tanh\left(\frac{y-0.8}{2\sqrt{2}\varepsilon}\right)\right] - \phi_1(x,y,0) \tag{42}$$

$$\phi_3(x,y,0) = \frac{1}{2}\left[\tanh\left(\frac{y-0.8}{2\sqrt{2}\varepsilon}\right) - \tanh\left(\frac{y-2.5}{2\sqrt{2}\varepsilon}\right)\right] \tag{43}$$

$$\phi_4(x,y,0) = 1-\phi_1(x,y,0)-\phi_2(x,y,0)-\phi_3(x,y,0) \tag{44}$$

On the left and right boundaries, the periodic boundary condition is used for the pressure. On the top and bottom boundaries, we use a more accurate pressure boundary condition proposed by Lee et al. (2011). The density ratio is $\rho_1 : \rho_2 : \rho_3 : \rho_4 = 1 : 4 : 3 : 2$, the viscosity ratio is $\eta_1 : \eta_2 : \eta_3 : \eta_4 = 1 : 1 : 1 : 1$. The gravitational acceleration is $\mathbf{g} = (0, -g)$. The schematic illustration of initial conditions is shown in Fig. 16. In the simulations, we set $\Delta t = 0.1h$, $h = 1/64$, $Re = 30$, $g = 1$, $Fr = 1$, $\varepsilon = \varepsilon_4$, $Pe = 0.01/\varepsilon$, $We_{12} = 30$, $We_{13} = 20$, $We_{23} = 15$, $We_{24} = 1$, and $We_{34} = 60$. The top, middle, and bottom rows of Fig. 17 display the time evolutions of rising bubble with respect to $We_{14} = 0.36$, 0.12, and 0.04, respectively. The Weber number We_{14}, which relates to the relative magnitude of inertial and surface tension force at the interface between fluid 1 and 4, is expected to affect the dynamics of rising bubble.

From Fig. 17, we observe that the light bubble rises up and deforms. When the bubble penetrates the interface between fluid 2 and 3, the fluid 2 adheres to bubble and undergoes a large deformation because the surface tension forces on three fluid interfaces are relatively weak. Until $t = 14.0625$, the dynamics of each case is same: the thin film of fluid 2 covers the top of bubble at $t = 1.4063$, after the bubble penetrates the interface between fluid 2 and 3, the fluid 2 adheres to the rear of bubble. With the upward movement of bubble, the fluid 2 is obviously stretched. After the bubble is totally immersed into fluid 3, the buoyancy force makes the bubble rises and reaches the interface between fluid 3 and 4 at $t = 14.0625$. After $t = 14.0625$, the top row of Fig. 17 shows that the departure of bubble has appeared at $t = 22.5$. Later, the bubble rises up in fluid 4. Because the surface tension force between bubble and fluid 4 is larger than that between bubble and fluid 3, it can be observed that the bubble in fluid 4 does not deform a lot. From the middle of Fig. 17, the stronger surface tension force delays the rising bubble. At $t = 22.5$, the fluid 3 still adheres to the rear of bubble and the departure appears at $t = 25.3125$. The bottom row of Fig. 17 shows the case with the strongest surface tension force between bubble and fluid 4. We observe that the bubble reaches the interface between fluid 3 and 4 at $t = 19.6875$, then the bubble is captured between two fluid layers all along. This phenomenon indicates that the surface tension force is greater than the buoyancy force.

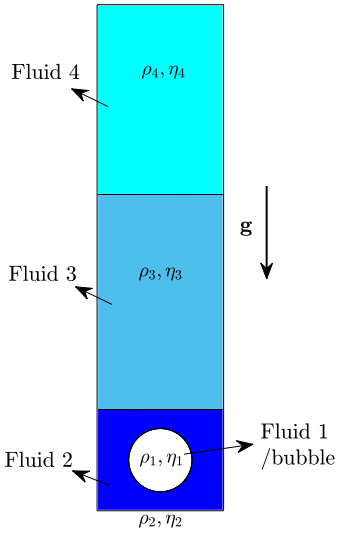

Fig. 16. Schematic illustration of rising bubble in a four-component fluid system.

To show the effect of different viscosities, we implement the simulation with same initial conditions and parameters except $We_{14} = 0.36$ and $\eta_1 : \eta_2 : \eta_3 : \eta_4 = 1 : 1 : 2 : 0.25$. The time evolution of rising bubble is shown in Fig. 18. Before the bubble penetrate the interface between fluid 2 and fluid 3, the dynamics is similar with that shown in the top row of Fig. 17. Since the viscosity of fluid 3 is greater, the bubble rises in fluid 3 with less deformation. After the bubble crosses the interface between fluid 3 and fluid 4, the lower viscosity of fluid 4 makes the bubble rises rapidly and be more flattened than that shown in the top row of Fig. 17.

To show the surface tension effects of interface between fluid 3 and fluid 4, we set $We_{12} = 30$, $We_{13} = 20$, We_{14}

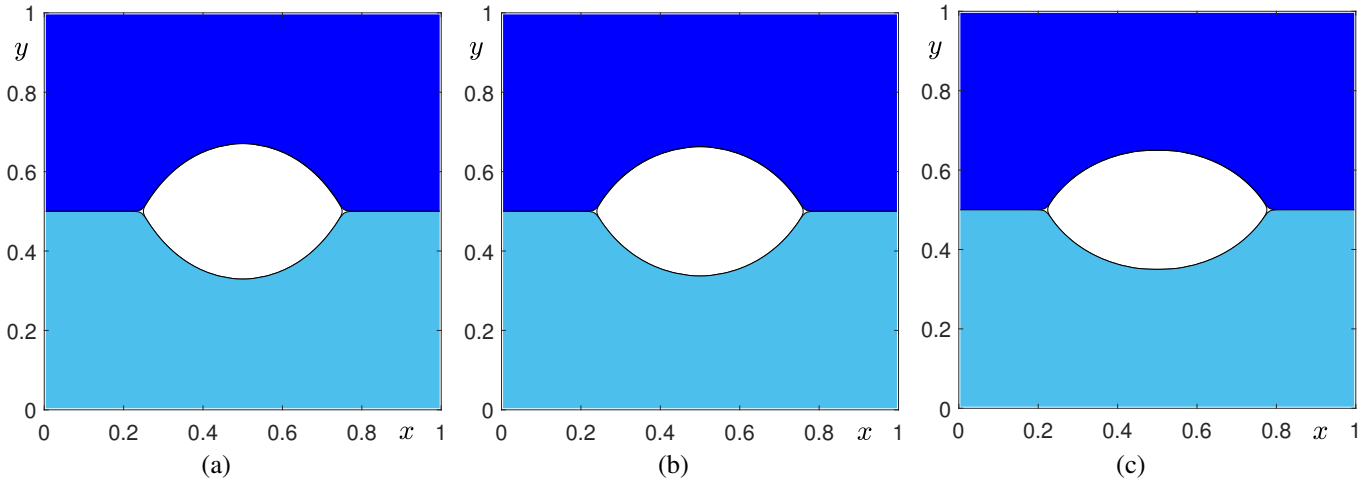

Fig. 14. Equilibrium states of liquid lens with respect to (a) $\sigma_{12}:\sigma_{13}:\sigma_{23}=1.4:1:1.4$, (b) $\sigma_{12}:\sigma_{13}:\sigma_{23}=1.2:1:1.2$, and (c) $\sigma_{12}:\sigma_{13}:\sigma_{23}=1:1:1$.

Table 4. Comparison with exact and numerical lengthes of liquid lens.

σ_{12}	Exact d	d, Present model	d, NCLS-FEST	d, NCLS-CSF
1.4	0.5014	0.5003	0.4975	0.4957
1.2	0.5220	0.5194	0.5170	0.5129
1	0.5540	0.5517	0.5458	0.5397

= 60, We_{23} = 15, and We_{24} = 1. We choose three different values of We_{34} = 0.04, 0.12, and 0.36. Other parameters keep unchanged. Fig. 19 shows the snapshots of raising bubble with respect to We_{34} = 0.04, 0.12, and 0.36, respectively. As we can see, with the decrease of surface tension of interface between fluid 3 and fluid 4, the bubble raises fast into fluid 4.

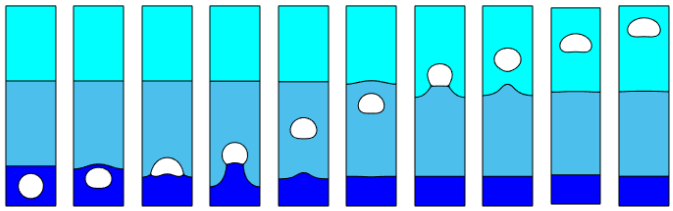

Fig. 18. Time evolution of rising bubble with We_{14} = 0.36 and $\eta_1:\eta_2:\eta_3:\eta_4=1:1:2:0.25$. From the left to right, the results are at t = 0, 1.4063, 2.8125, 5.625, 9.8438, 14.0625, 19.6875, 22.5, 25.3125, and 28.125.

4.8 Droplet impacting on a thin liquid film

In this subsection, we present an example of droplet impacting on a thin liquid film to further validate the present model in dealing with multi-phase fluid flows with large density ratio, large viscosity ratio and high Reynolds number. As shown in Fig. 20, the configuration of this physical problem is a droplet (fluid 1) hitting thin liquid film (fluid 2) with an initial velocity, the densities and viscosities of droplet and thin liquid film are significantly larger than those of ambient fluid (fluid 3). The computational domain is set to be $\Omega=(0,4)\times(0,1)$ and the mesh size is 256×64, i.e., h = 1/64. The initial conditions of velocities and phase-field functions are defined as:

$$\phi_1(x,y,0)=\frac{1}{2}\left[1+\tanh\left(\frac{0.3-\sqrt{(x-2)^2+(y-0.4)^2}}{2\sqrt{2}\varepsilon}\right)\right] \tag{45}$$

$$\phi_2(x,y,0)=\frac{1}{2}\left[1+\tanh\left(\frac{0.1-y}{2\sqrt{2}\varepsilon}\right)\right] \tag{46}$$

$$\phi_3(x,y,0)=1-\phi_1(x,y,0)-\phi_2(x,y,0)$$

$$u(x,y,0)=0,\quad v(x,y,0)=-V\phi_1(x,y,0) \tag{47}$$

Here, V = 2 represents the magnitude of impacting velocity.

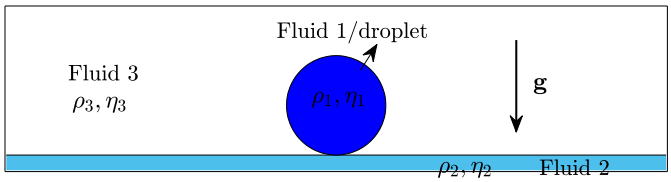

Fig. 20. Schematic illustration of the initial condition of droplet impacting a thin liquid film.

We set $\Delta t=0.00625h$, $\varepsilon=\varepsilon_{3.5}$, $Pe=0.1/\varepsilon$, Fr = 1, We_{12} = We_{13} = We_{23} = 1. The gravity is $\mathbf{g}=(0,-g)$ and g = 1. The density is $\rho_1:\rho_2:\rho_3=95:100:1$ and the viscosity ratio is $\eta_1:\eta_2:\eta_3=95:100:1$. In the first case, we use a relatively lower Reynolds number Re = 100 and implement the simulation until t = 0.3418. The snapshots at different computational moments are shown in Fig. 21. In the second

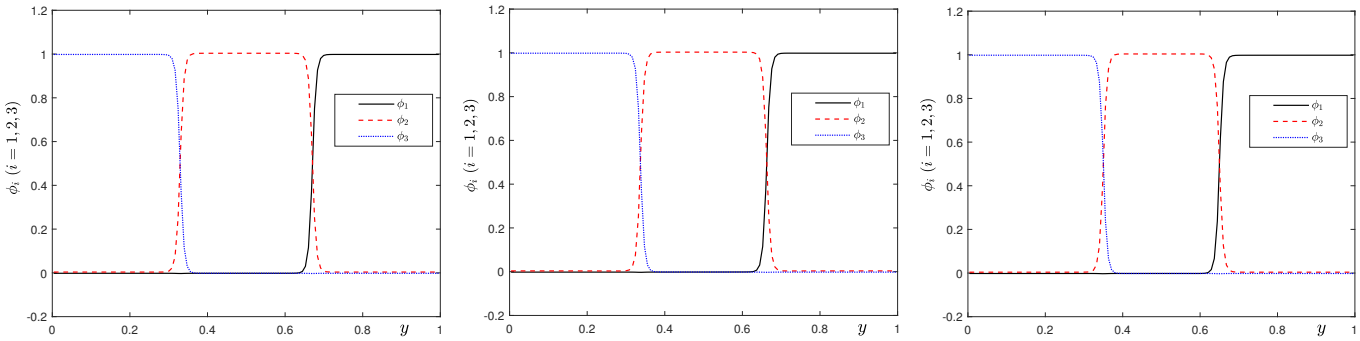

(a) (b) (c)

Fig. 15. Cross sections of equilibrium phase-field functions along $x = 0.5$. Here, (a), (b), and (c) correspond to $\sigma_{12} : \sigma_{13} : \sigma_{23}$ = 1.4 : 1 : 1.4, 1.2 : 1 : 1.2, and 1 : 1 : 1, respectively.

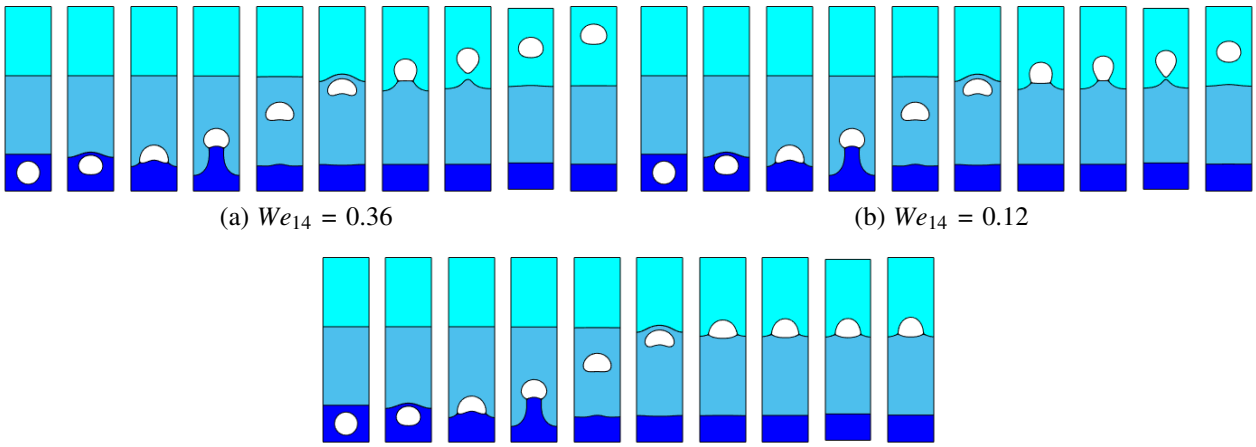

(a) We_{14} = 0.36 (b) We_{14} = 0.12

(c) We_{14} = 0.04

Fig. 17. Time evolutions of rising bubble with respect to We_{14} = 0.36 (top), We_{14} = 0.12 (middle), and We_{14} = 0.04 (bottom). From the left to right, the results are at t = 0, 1.4063, 2.8125, 5.625, 9.8438, 14.0625, 19.6875, 22.5, 25.3125, and 28.125.

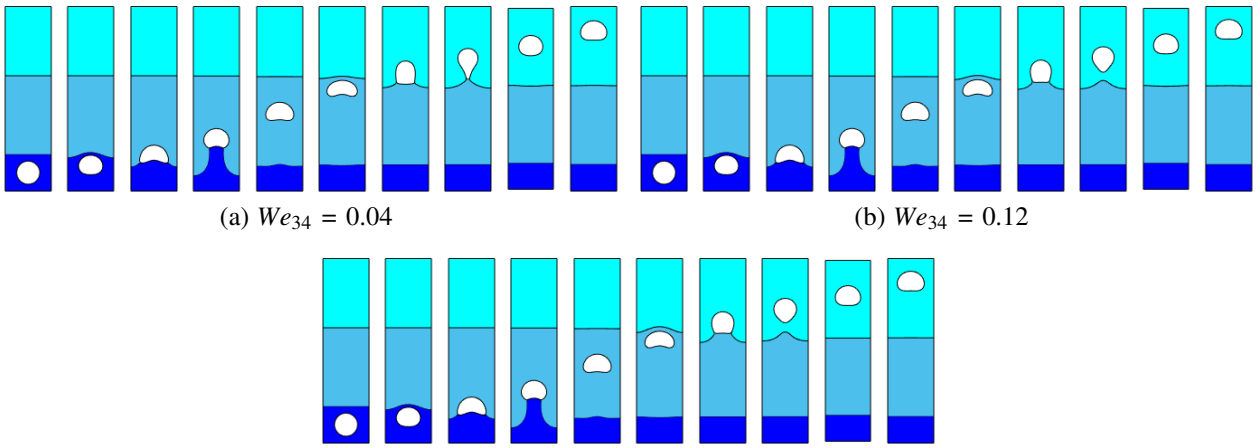

(a) We_{34} = 0.04 (b) We_{34} = 0.12

(c) We_{34} = 0.36

Fig. 19. Time evolutions of rising bubble with respect to We_{34} = 0.04 (top), We_{34} = 0.12 (middle), and We_{34} = 0.36 (bottom). From the left to right, the results are at t = 0, 1.4063, 2.8125, 5.625, 9.8438, 14.0625, 19.6875, 22.5, 25.3125, and 28.125.

and third cases, we perform the similar simulations by using Re = 1,000 and 10,000, respectively. The associated results are displayed in Figs. 22 and 23. For the case with Re = 100, the deformation of droplet towards outward forces the splashing of liquid film. When we increase the Reynolds number to Re = 1,000, the low fluid viscosity leads to more obvious splashing of liquid film. We observe that the ends of splashing liquid become thinner than those in Fig. 21. When the Reynolds number is increased to Re = 10,000, the dynamic phenomenon is similar with that in Fig. 22 until t = 0.2393. At t = 0.3418, the pinch-off appears at the ends of splashing liquid due to the weakest effect of fluid viscosity.

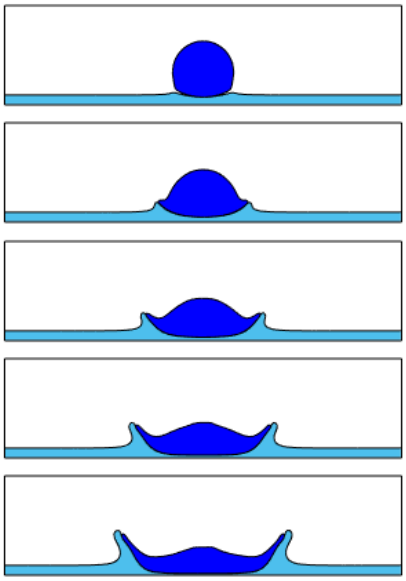

Fig. 21. Time evolution of droplet impacting on a thin liquid film with Re = 100. From the top to bottom, the results are at t = 0.0342, 0.1025, 0.1709, 0.2393, and 0.3418.

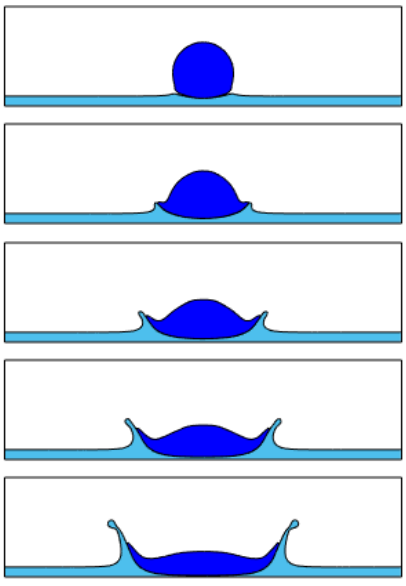

Fig. 22. Time evolution of droplet impacting on a thin liquid film with Re = 1,000. From the top to bottom, the results are at t = 0.0342, 0.1025, 0.1709, 0.2393, and 0.3418.

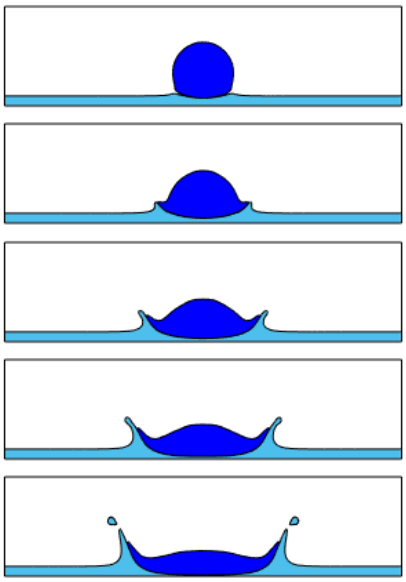

Fig. 23. Time evolution of droplet impacting on a thin liquid film with Re = 10,000. From the top to bottom, the results are at t = 0.0342, 0.1025, 0.1709, 0.2393, and 0.3418.

To show the effect of thickness of liquid film, we implement the simulations by setting the the height of initial liquid film be 0.05 and 0.15. The size of droplet, initial velocity, and parameters are unchanged. Figs. 24 and 25 show the evolutional results with respect to different thicknesses of liquid film. When the thickness of liquid film is 0.05, the droplet splashes upwards to generate the pinch-off phenomena. At final stage, the splashing of liquid film is delayed. When the thickness of liquid film is 0.15, the liquid film first splashes upwards to generate the pinch-off droplets. At final stage, the splashing of liquid film is more obvious.

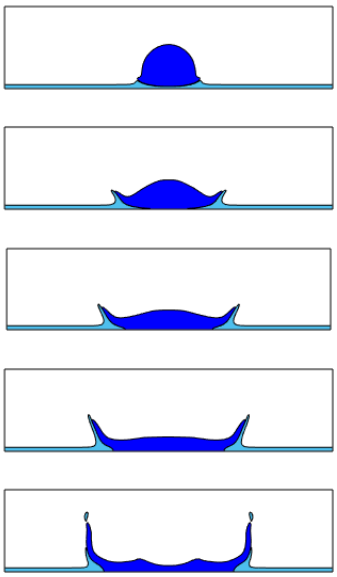

Fig. 24. Time evolution of droplet impacting on a thin liquid film. The thickness of liquid film is 0.05. From the top to bottom, the results are at t = 0.0342, 0.1025, 0.1709, 0.2393, and 0.3418.

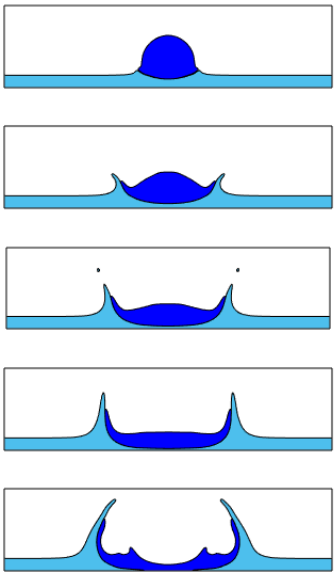

Fig. 25. Time evolution of droplet impacting on a thin liquid film. The thickness of liquid film is 0.15. From the top to bottom, the results are at t = 0.0342, 0.1025, 0.1709, 0.2393, and 0.3418.

Finally, we implement a 3D simulation in $\Omega = (0,4) \times (0,4) \times (0,1)$. The mesh grids along x-, y-, and z-directions are 256, 256 and 64, respectively. Along x- and y-directions, all variables are periodic. On the top and bottom boundaries, the velocities are zero. The homogeneous-Neumann boundary condition is used for pressure and phase-field functions:

$$\phi_1(x,y,z,0) = \frac{1}{2}\left[1+\tanh\left(\frac{0.3-\sqrt{(x-2)^2+(y-2)^2+(z-0.4)^2}}{2\sqrt{2}\varepsilon}\right)\right] \tag{48}$$

$$\phi_2(x,y,z,0) = \frac{1}{2}\left[1+\tanh\left(\frac{0.1-z}{2\sqrt{2}\varepsilon}\right)\right] \tag{49}$$

$$\phi_3(x,y,z,0) = 1-\phi_1(x,y,z,0)-\phi_2(x,y,z,0) \tag{50}$$

$$u(x,y,z,0) = 0,\ v(x,y,0) = 0,\ w(x,y,z,0) = -W\phi_1(x,y,z,0) \tag{51}$$

Fig. 26 illustrates the initial conditions. Here, W = 3 is the magnitude of impacting velocity. The parameters are set to be Δt = 0.025h, h = 1/64, Re = 10,000, $\varepsilon = \varepsilon_{3.5}$, Pe = 0.3/ε, Fr = 1, $We_{12} = We_{13} = We_{23}$ = 1. The gravity is $\mathbf{g} = (0,-g)$ and g = 1. The density is $\rho_1 : \rho_2 : \rho_3 = 95 : 100 : 1$ and the viscosity ratio is $\eta_1 : \eta_2 : \eta_3 = 95 : 100 : 1$. In Fig. 27, the results at different computational moments are displayed. After the droplet impacts the liquid film, the deformation of droplet forces the liquid to splash upwards. With the evolution of splashing, an obvious cavity can be observed. Moreover, the low viscosity of fluid leads to the instability on the ends of splashing liquid. Finally, the pinch-off phenomenon appears and a liquid ring is left. In 3D space, the splashing dynamics is different from that in 2D space due to more complex effects of surface tension force and buoyancy force.

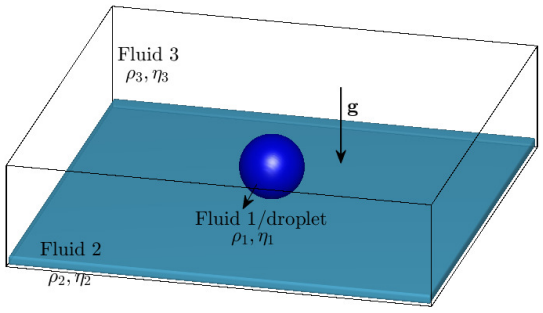

Fig. 26. Schematic illustrations of droplet impacting on a thin liquid film in 3D space.

5. Conclusions

This work presented an improved version of generalized surface tension force formulation which was original proposed by Kim (2009). Using an equilibrium interface condition, we derived the expression of a signed-distance function which was associated with i-th fluid concentration. The curvature calculated with signed-distance function was more accurate. When the thickness of diffuse interface became sharp, the present surface tension force model significantly suppressed the increase of spurious velocity. Similar with Kim's model (Kim, 2009), the present model was also general because it was possible to describe any combination of fluid interfaces without specific criterions. Extensive numerical simulations were implemented to verify the capability of proposed model. The test of liquid lens showed that the present model could accurately simulate the spreading length of lens. The resulting results are comparable with those computed by conservative level set method. The effect of surface tension force was investigated by simulating the rising bubble in a four-component fluid system. Finally, the droplet impacting on a thin liquid film was simulated to show the good performance in the cases with large density ratio and high Reynolds number.

Acknowledgements

Junxiang Yang is supported by the Macau Science and Technology Development Fund (FDCT) (No. FDCT-24-080-SCSE).

Conflict of interest

The authors declare no competing interest.

References

Aihara, S., Takada, N., Takaki, T. Highly conservative Allen-Cahn-type multi-phase-field model and evaluation of its accuracy. Theoretical and Computational Fluid Dynamics, 2023, 37(5): 639-659.

Bi, Y., Qin, L., Yu, L., et al. Interactions between a toroidal bubble and a free surface. Journal of Fluid Mechanics, 2024, 998: A28.

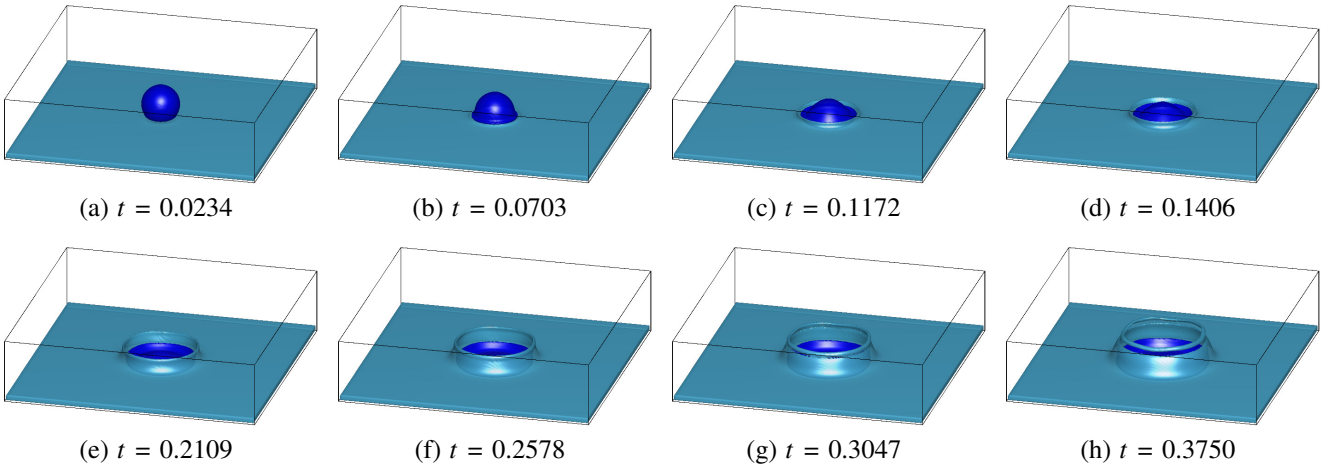

(a) t = 0.0234 (b) t = 0.0703 (c) t = 0.1172 (d) t = 0.1406

(e) t = 0.2109 (f) t = 0.2578 (g) t = 0.3047 (h) t = 0.3750

Fig. 27. Simulation of 3D droplet impacting on a thin liquid film. The computational moments are shown under each figure.

Brackbill, J. U., Kothe, D. B., Zemach, C. A continuum method for modeling surface tension. Journal of computational physics, 1992, 100(2): 335-354.

Chen, Y., Yu, B., Lu, W., et al. Review on numerical simulation of boiling heat transfer from atomistic to mesoscopic and macroscopic scales. International Journal of Heat and Mass Transfer, 2024, 225: 125396.

Caltagirone, J. P. Application of discrete mechanics model to jump conditions in two-phase flows. Journal of Computational Physics, 2021, 432: 110151.

Cho, H., Kang, M. Fully implicit and accurate treatment of jump conditions for two-phase incompressible Navier-Stokes equations. Journal of Computational Physics, 2021, 445: 110587.

Chiu, P. A coupled phase field framework for solving incompressible two-phase flows. Journal of Computational Physics, 2019, 392: 115-140.

Chiu, P. H., Lin, Y. T. A conservative phase field method for solving incompressible two-phase flows. Journal of Computational Physics, 2011, 230(1): 185-204.

Choi, J. W., Lee, H. G., Jeong, D., et al. An unconditionally gradient stable numerical method for solving the Allen-Cahn equation. Physica A: Statistical Mechanics and its Applications, 2009, 388(9): 1791-1803.

Connington, K., Lee, T. A review of spurious currents in the lattice Boltzmann method for multiphase flows. Journal of mechanical science and technology, 2012, 26(12): 3857-3863.

Dong, S. An efficient algorithm for incompressible N-phase flows. Journal of Computational Physics, 2014, 276: 691-728.

Dong, S. Physical formulation and numerical algorithm for simulating N immiscible incompressible fluids involving general order parameters. Journal of Computational Physics, 2015, 283: 98-128.

Dong, S. Wall-bounded multiphase flows of N immiscible incompressible fluids: Consistency and contact-angle boundary condition. Journal of Computational Physics, 2017, 338: 21-67.

Di, Y., Li, R., Tang, T. A general moving mesh framework in 3D and its application for simulating the mixture of multi-phase flows. Communications in Computational Physics, 2008, 3(3): 582-602.

Goulding, J., Ayazi, M., Shinar, T., et al. Simplified conservative discretization of the Cahn-Hilliard-Navier-Stokes equations, Journal of Computational Physics, 2024, 519: 113382.

Ganesan, S., Matthies, G., Tobiska, L. On spurious velocities in incompressible flow problems with interfaces. Computer Methods in Applied Mechanics and Engineering, 2007, 196(7): 1193-1202.

Howard, A. A., Tartakovsky, A. M. A conservative level set method for N-phase flows with a free-energy-based surface tension model. Journal of Computational Physics, 2021, 426: 109955.

Hwang, H., Jain, S. S. A robust phase-field method for two-phase flows on unstructured grids. Journal of Computational Physics, 2024, 507: 112972.

Hong, Q., Zhao, J. A physics-informed structure-preserving numerical scheme for the phase-field hydrodynamic model of ternary fluid flows. Numerical Mathematics: Theory, Methods and Applications, 2023, 16(3): 565-596.

Jain, S. Accurate conservative phase-field method for simulation of two-phase flows. Journal of Computational Physics, 2022, 469: 111529.

Kim, J. A continuous surface tension force formulation for diffuse-interface models. Journal of computational physics, 2005, 204(2): 784-804.

Kim, J. Phase field computations for ternary fluid flows. Computer methods in applied mechanics and engineering, 2007, 196(45-48): 4779-4788.

Kim, J. A generalized continuous surface tension force formulation for phase-field models for multi-component immiscible fluid flows. Computer Methods in Applied Mechanics and Engineering, 2009, 198(37-40): 3105-3112.

Kim, J. An augmented projection method for the incompressible navier-stokes equations in arbitrary domains.

International Journal of Computational Methods, 2005, 2(2): 201-212.

Kim, J. Phase-field models for multi-component fluid flows. Communications in Computational Physics, 2012, 12(3): 613-661.

Li, Y., Yun, A., Lee, D., et al. Three-dimensional volume-conserving immersed boundary model for two-phase fluid flows. Computer Methods in Applied Mechanics and Engineering, 2013, 257: 36-46.

Liu, H., Ng, C. S., Chong, K. L., et al. An efficient phase-field method for turbulent multiphase flows. Journal of computational physics, 2021, 446: 110659.

Lee, H. G., Kim, J. An efficient numerical method for simulating multiphase flows using a diffuse interface model. Physica A: Statistical Mechanics and its Applications, 2015, 423: 33-50.

Li, Y., Choi, J. I., Kim, J. A phase-field fluid modeling and computation with interfacial profile correction term. Communications in Nonlinear Science and Numerical Simulation, 2016, 30(1-3): 84-100.

Lee, H. G., Kim, K., Kim, J. On the long time simulation of the Rayleigh–Taylor instability. International journal for numerical methods in engineering, 2011, 85(13): 1633-1647.

Landau, L. D., Lifshitz, E. M. Fluid Mechanics, Pergamon Press, Oxford, 1987.

Mu, K., Qiao, R., Ding, H., et al. Modulation of coaxial cone-jet instability in active co-flow focusing. Journal of Fluid Mechanics, 2023, 977: A14.

Nightingale, A. M., Phillips, T. W., Bannock, J. H., et al. Controlled multistep synthesis in a three-phase droplet reactor. Nature communications, 2014, 5(1): 3777.

Olsson, E., Kreiss, G. A conservative level set method for two phase flow. Journal of computational physics, 2005, 210(1): 225-246.

Olsson, E., Kreiss, G., Zahedi, S. A conservative level set method for two phase flow II. Journal of Computational Physics, 2007, 225(1): 785-807.

Oshima, N., Tabe, Y. Reduction of spurious velocity in the free-energy-based lattice Boltzmann method for large density ratio. Journal of Thermal Science and Technology, 2015, 10(1): JTST0004.

Rosca, I. D., Watari, F., Uo, M. Microparticle formation and its mechanism in single and double emulsion solvent evaporation. Journal of Controlled Release, 2004, 99(2): 271-280.

Setu, S. A., Dullens, R. P., Hernández-Machado, A., et al. Superconfinement tailors fluid flow at microscales. Nature communications, 2015, 6(1): 7297.

Shen, J., Yang, X. Energy stable schemes for Cahn-Hilliard phase-field model of two-phase incompressible flows. Chinese Annals of Mathematics, Series B, 2010, 31(5): 743-758.

Smith, K. A., Solis, F. J., Chopp, D. A projection method for motion of triple junctions by level sets. Interfaces and free boundaries, 2002, 4(3): 263-276.

Tryggvason, G., Bunner, B., Esmaeeli, A., et al. A front-tracking method for the computations of multiphase flow. Journal of computational physics, 2001, 169(2): 708-759.

Tornberg, A. K., Engquist, B. A finite element based level-set method for multiphase flow applications. Computing and Visualization in Science, 2000, 3(1): 93-101.

Trottenberg, U., Oosterlee, C. W., Schüller, A. Multigrid, London, Academic Press, 2001.

Wang, Z., Zheng, X., Chryssostomidis, C., et al. A phase-field method for boiling heat transfer. Journal of computational physics, 2021, 435: 110239.

Wang, Z., Xu, P., Zuo, Z., et al. Effect of liquid elasticity on transient cavitation bubbles in the tube. Physics of Fluids, 2024, 36(8): 081702.

Wagner, A. J. The origin of spurious velocities in lattice Boltzmann. International Journal of Modern Physics B, 2003, 17(01n02): 193-196.

Xiao, X., Feng, X., Li, Z. The local tangential lifting method for moving interface problems on surfaces with applications. Journal of Computational Physics, 2021, 431: 110146.

Xia, Q., Yang, J., Li, Y. On the conservative phase-field method with the N-component incompressible flows. Physics of Fluids, 2023, 35(1): 012120.

Yuan, H., Chen, Z., Shu, C., et al. A free energy-based surface tension force model for simulation of multiphase flows by level-set method. Journal of Computational Physics, 2017, 345: 404-426.

Yang, J., Han, H., Liu, S., et al. Efficiently and consistently energy-stable L2-phase-field method for the incompressible ternary fluid problems. Physica D: Nonlinear Phenomena, 2024, 470: 134346.

Yang, Z., Dong, S. Multiphase flows of N immiscible incompressible fluids: an outflow/open boundary condition and algorithm. Journal of Computational Physics, 2018, 366: 33-70.

Zhu, Z. C., Liu, H. R., et al. Buoyancy-driven bubbles in a constricted vertical capillary. Physics of Fluids, 2022, 34(3): 032102.

Zhang, Z., Zhang, C, Liu, H, et al. Impact dynamics of compound drops of fluids with density contrast. Journal of Fluid Mechanics, 2023, 964: A34.

Zhao, J., Han, D. Second-order decoupled energy-stable schemes for Cahn-Hilliard-Navier-Stokes equations. Journal of Computational Physics, 2021, 443: 110536.

Zhu, G., Kou, J., Yao, J., et al. A phase-field moving contact line model with soluble surfactants. Journal of Computational Physics, 2020, 405: 109170.